

High- Q Nanophotonics over the Full Visible Spectrum Enabled by Hexagonal Boron Nitride Metasurfaces

Lucca Kühner, Luca Sortino, Benjamin Tilmann, Thomas Weber, Kenji Watanabe, Takashi Taniguchi, Stefan A. Maier, and Andreas Tittl*

All-dielectric optical metasurfaces with high quality (Q) factors have been hampered by the lack of simultaneously lossless and high-refractive-index materials over the full visible spectrum. In fact, the use of low-refractive-index materials is unavoidable for extending the spectral coverage due to the inverse correlation between the bandgap energy (and therefore the optical losses) and the refractive index (n). However, for Mie resonant photonics, smaller refractive indices are associated with reduced Q factors and low mode volume confinement. Here, symmetry-broken quasi bound states in the continuum (qBICs) are leveraged to efficiently suppress radiation losses from the low-index ($n \approx 2$) van der Waals material hexagonal boron nitride (hBN), realizing metasurfaces with high- Q resonances over the complete visible spectrum. The rational use of low- and high-refractive-index materials as resonator components is analyzed and the insights are harnessed to experimentally demonstrate sharp qBIC resonances with Q factors above 300, spanning wavelengths between 400 and 1000 nm from a single hBN flake. Moreover, the enhanced electric near fields are utilized to demonstrate second-harmonic generation with enhancement factors above 10^2 . These results provide a theoretical and experimental framework for the implementation of low-refractive-index materials as photonic media for metaoptics.

amplitude,^[3,4] directionality of light scattering,^[5,6] spin,^[7,8] and orbital angular momentum^[9,10] without the limitations of intrinsic material losses as for metal-based approaches. In particular, applications driven by near-field enhancement, such as biomolecular sensing, rely on high resonance quality (Q) factors (defined as resonance wavelength divided by line width), and hence high electromagnetic near-field intensities to achieve maximum specimen sensitivity.^[11,12] The inherent correlation between the resonance quality factor and the resonator refractive index^[13] known from, for example, Mie theory, thus led to the advance of all-dielectric nanophotonics based on high-refractive-index material systems, such as silicon,^[14,15] germanium,^[16,17] or gallium phosphide.^[18,19] Although these materials offer great properties for high- Q resonances in the near-infrared (NIR) and infrared (IR) spectral region, they are accompanied by high material-intrinsic interband absorption losses throughout the visible spectral range due to their intermediate bandgap energies. Owing to these fundamental material limitations, lossless high-index materials throughout the complete visible spectral range are lacking.^[20–23] In particular, for the visible wavelength range, there exists a competition between a large bandgap for lossless


1. Introduction

All-dielectric materials have recently emerged in nanophotonics as a key ingredient to control the properties of light at the nanoscale, such as the phase,^[1,2] near-field

traversal range due to their intermediate bandgap energies. Owing to these fundamental material limitations, lossless high-index materials throughout the complete visible spectral range are lacking.^[20–23] In particular, for the visible wavelength range, there exists a competition between a large bandgap for lossless

L. Kühner, L. Sortino, B. Tilmann, T. Weber, S. A. Maier, A. Tittl
Chair in Hybrid Nanosystems
Nanoinstitute Munich, and Center for NanoScience
Faculty of Physics
Ludwig-Maximilians-University Munich
Königinstraße 10, 80539 München, Germany
E-mail: andreas.tittl@physik.uni-muenchen.de
K. Watanabe
Research Center for Functional Materials
National Institute for Materials Science
1-1 Namiki, Tsukuba 305-0044, Japan

T. Taniguchi
International Center for Materials Nanoarchitectonics
National Institute for Materials Science
1-1 Namiki, Tsukuba 305-0044, Japan
S. A. Maier
School of Physics and Astronomy
Monash University
Wellington Rd, Clayton, VIC 3800, Australia
S. A. Maier
The Blackett Laboratory
Department of Physics
Imperial College London
London SW7 2AZ, UK

 The ORCID identification number(s) for the author(s) of this article can be found under <https://doi.org/10.1002/adma.202209688>.

© 2023 The Authors. Advanced Materials published by Wiley-VCH GmbH. This is an open access article under the terms of the Creative Commons Attribution License, which permits use, distribution and reproduction in any medium, provided the original work is properly cited.

DOI: 10.1002/adma.202209688

photonics and a high refractive index of the material for better optical mode confinement and higher Q factors. This physical limitation is mathematically described by the Hervé equation:^[21]

$$n = \sqrt{1 + \left(\frac{A}{E_g + B} \right)^2} \quad (1)$$

where the refractive index n of the material is correlated with its bandgap energy E_g , where A ($= 13.6$ eV) and B ($= 3.4$ eV) are constants. In order to obtain high- Q resonances in the visible (400–800 nm) without substantial material losses, a bandgap of 3.54 eV (≈ 350 nm) is required, limiting the maximum refractive index available to $n = 2.2$ according to Equation (1). In fact, due to the lack of high-index and lossless materials in the visible, experimental demonstrations of high- Q resonances in the blue (i.e., below 460 nm) are still missing.^[24] Owing to the low refractive index of the materials, and thus low quality factors of the associated Mie resonances within these materials, this avenue is mostly unexplored.^[25,26]

In addition to intrinsic material losses, resonances in nanostructured dielectrics are affected by a radiative loss channel, which becomes dominant when the refractive index contrast between resonator and the environment decreases. Photonic bound states in the continuum (BICs) provide a unique pathway for tailoring radiative losses in addition to the refractive-index-based effects discussed above. Symmetry-broken quasi-BIC (qBIC) metasur-

faces in particular offer precise and straightforward control over the (radiative) Q factor of the resonances via the geometrical asymmetry of the constituent unit cell building blocks,^[27,28] which sets them apart from other BIC implementations based on accidental far-field destructive interference^[29] or strong mode coupling.^[30,31] Initiated by the versatility of the BIC concept, they open up a new avenue for the usage of low-index lossless materials, especially for realizing high- Q resonances throughout the visible spectral range.

Hexagonal boron nitride (hBN),^[32] a 2D van der Waals (vdW) material, exhibits an indirect bandgap of 5.95 eV^[33] with an average refractive index of $n = 2.0$, potentially enabling photonic applications down to the ultraviolet (UV) range.^[34,35] So far, it was mainly used as insulating or encapsulation layer in electronics and photonics,^[36–38] but also found optical applications in a small spectral window (the so-called Reststrahlen band) in the IR due to its strong phononic excitations.^[39–42] The few demonstration in the visible have focused on photonic crystal cavities or extended ring resonators,^[43,44] which either require suspension or large spatial footprints and have not demonstrated resonances below 580 nm. Nevertheless, its optical properties along with the monocrystalline material quality and compatibility with other 2D materials^[45] renders hBN invaluable for the realization of photonic resonances throughout the visible as a basis for enhanced light–matter interaction that has so far been challenging in this spectral range. Beneficially, mechanically exfoliated bulk hBN is obtained in monocrystalline quality, thus diminishing the need for expensive deposition tools and fine engineering of deposition parameters, while simultaneously boosting the quality factors of the resonant modes due to the reduced intrinsic material losses.

In this work, based on a careful analysis of the underlying physics associated with symmetry-broken qBICs in low index

resonators, we experimentally demonstrate that hBN-based metasurfaces with a low refractive index can support high- Q qBIC resonances covering the whole visible spectrum. Our results greatly extend the operational wavelength range for all-dielectric metasurfaces, especially providing high- Q resonances in the blue part of the electromagnetic spectrum for the first time, all within a single sample fabricated from an hBN crystal with constant resonator height. From our numerical investigation, we find that the resonantly enhanced electric near fields are concentrated inside the resonators. Hence, we harness these highly enhanced electromagnetic near fields to demonstrate a 388-fold enhancement for the material-intrinsic second-harmonic generation (SHG) in hBN. Because of its combination affinity with other 2D materials, the presence of native single photon sources, and its general optical and chemical properties, our results provide a new paradigm for the development of novel vdW nanophotonic platforms.

2. High- Q Resonances from Low-Refractive-Index Materials

Owing to its large bandgap energy and thus low losses in the visible spectrum, our goal is to obtain sharp resonances from hBN in the complete visible and NIR spectral range (400–1000 nm). For the description of the hBN optical properties, we utilize a model based on Sellmaier's equations for both the in-plane n_i and out-of-plane n_o refractive index^[46] which accounts for the high material anisotropy. The resulting dispersion for both material axes is depicted on the right-hand side of **Figure 1A** and is utilized to model the material properties in our numerical calculations.

In order to analyze symmetry-broken qBIC metasurfaces composed of hBN, we employ a double rod unit cell. Here, the symmetry breaking is introduced by shortening one rod with respect to the other, such that the geometrical asymmetry is given as $\Delta L = L_2 - L_1$. The asymmetric rod qBIC unit cell is schematically depicted in **Figure 1B**, with initially fixed geometry settings (periodicities $p_y = p_x + 20$ nm = 430 nm, $L_2 = L_1 + \Delta L = 310 + 50$ nm, resonator height $h = 150$ nm, resonator width $w = 100$ nm) for a scaling factor $S = 1$. For the simulation of the transmittance spectra of our metasurfaces, we employ CST microwave studio that allows for the determination of the metasurface response in the frequency domain. In the simulation, we utilize periodic Floquet boundary conditions to calculate the scattering parameters of the metasurface yielding far-field quantities such as reflectance and transmittance. Furthermore, we assume plane-wave illumination and set the intrinsic hBN losses to zero within the spectral range of interest. Representative numerical spectra are shown on the right-hand side of **Figure 1B**. Unless stated differently, all the spectra shown in this manuscript are obtained for linear polarization along the long axis of the resonators. The resonance wavelength of the qBIC is controlled via fine and continuous scaling of the unit cell with a factor S , which yields closely spaced and sharp resonances throughout the visible to the NIR region.

Enabled by its large bandgap energy, hBN is an ideal candidate to realize high- Q resonances over the complete visible spectral range, outperforming other low-refractive-index

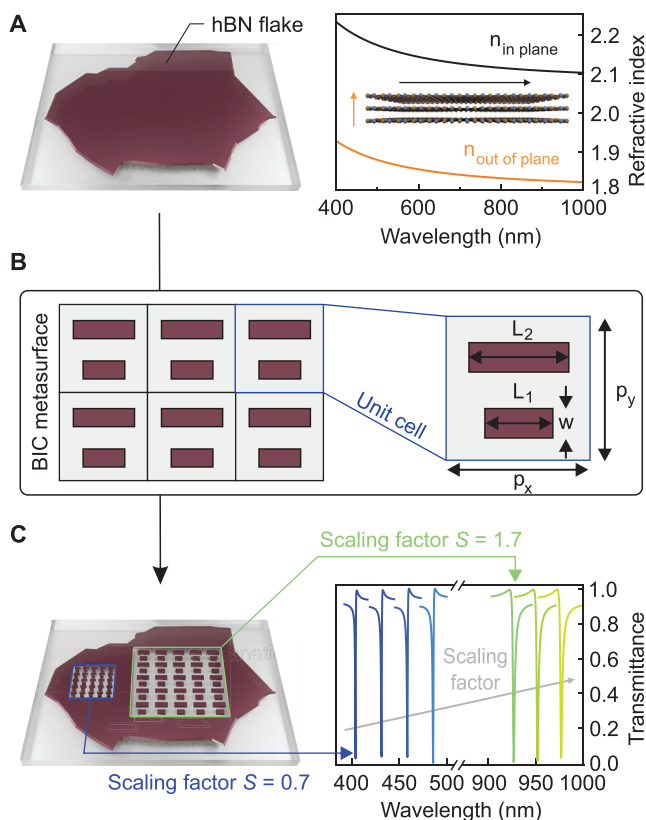


Figure 1. Hexagonal boron nitride metasurfaces for high- Q resonances in the visible. A) Left: schematic illustration of an exfoliated hBN flake on a transparent substrate used for the metasurface fabrication. Right: the corresponding refractive index data showing strong anisotropy within the hBN single crystal. B) Left: Schematic illustration of the qBIC metasurface. Right: Geometrical parameters used for the unit cell design. The unit cell is composed of two rods with different lengths $L_2 = L_1 + \Delta L = 310 + 50$ nm, a width of $w = 100$ nm, a resonator height $h = 150$ nm, and periodicities of $p_y = p_x + 20$ nm = 430 nm for a scaling factor $S = 1$. C) Left: schematics of the nanostructured qBIC metasurfaces patterned within the hBN. Right: pronounced high- Q resonances from the visible to the NIR by altering the scaling factor of the structures.

materials, such as titanium dioxide or silicon nitride, in the blue part of the visible spectrum. Most importantly, the resonance wavelength of hBN can be scaled to the IR and UV by further adjusting the scaling factor of the unit cell as indicated in numerical simulations in Figures S1 and S2, Supporting Information.

In order to demonstrate the feasibility of hBN as photonic resonator material enabled by the BIC concept, we perform in-depth numerical simulations, specifically investigating the influence of the refractive index of the dielectric resonator on the near- and far-field properties of the qBIC resonances. We consider resonators without a substrate to suppress Rayleigh anomalies that could influence the properties of the qBIC resonances, and set the resonator material as non-dispersive and lossless. Most importantly, the geometrical asymmetry ΔL of the system is adjusted based on the refractive index n of the resonator material to guarantee the same resonance Q factors for all refractive indices, assuming the generalized asymmetry (α) as:

$$\alpha = n \cdot \Delta L \quad (2)$$

This Q factor tunability is a defining property of symmetry-broken qBICs without which the accurate comparison of different resonator materials is infeasible.

A pronounced and spectrally isolated qBIC can be observed for all resonator refractive indices under consideration (Figure 2A). The refractive index spans a range from $n = 1.7$ to $n = 4.0$, mainly limited by the decreasing refractive index contrast to the substrate and fabrication limitations (gap sizes) at the lower end. We compare the $n = 4$ index value as a silicon representative and the $n = 2$ case for hBN in more detail, with the corresponding qBIC spectra depicted in Figure 2B. These qBIC resonances are associated with highly enhanced near fields (Figure 2C) with the typical qBIC pattern of oppositely oscillating dipoles in the x - y cross section. The maximum value of the electric near field outside the structures is larger for the Si resonator refractive index, whereas the electric field is more distributed and less localized for the case of hBN. By investigating the decay of the normalized electric field E_{norm} away from the structures in the z direction, we observe an exponential decay as depicted in Figure 2D for hBN (yellow dots) and silicon (purple dots). By fitting these data with an exponential decay function

$$E_{\text{norm}}(z) = \exp\left(-\frac{z}{\zeta}\right) \quad (3)$$

we extract the decay length ζ for both resonator materials by determining the distance for which the electric field drops to $1/e$ (red dashed line in Figure 2D) with respect to its value at the resonator surface. Indeed, the decay length for hBN-based resonators is roughly twice as large as for silicon-based resonators, indicating that the electric near field is more confined to the surface of the resonant structures in the Si case.

For a deeper understanding of the inherent differences between low-index- and high-index-based qBIC metasurfaces, we analyze the decay length as well as the mean and maximum electric fields inside and outside the resonators for a set of different resonator refractive indices as shown in Figure 2E. The investigation of the decay lengths shows a monotonous decrease toward a minimum value of around 40 nm for $n = 4$ (top panel in Figure 2E), related to the stronger confinements for higher index resonators.

For the investigation of the enhanced electric nearfields, we split the total field into a part inside and outside the resonators and calculate the mean and the maximum value, shown in the middle and bottom panels of Figure 2E. Notably, for increasing refractive indices, the electric fields are pushed outside the resonators as obvious from the higher maximum and mean values of the electric near fields outside the resonators. On the contrary, for smaller refractive indices, the electric field is rather located inside the resonators, rendering them ideally suited for material-intrinsic processes, such as high-harmonic generation or enhanced light-matter interaction utilizing hBN-encapsulated 2D materials. Furthermore, as a consequence of the strong dependence of the electric fields on the Q factor, the BIC-driven approach enables a precise tailoring of the electric fields via controlling the geometrical asymmetry of the metasurface. Moreover, qBIC metasurfaces based on

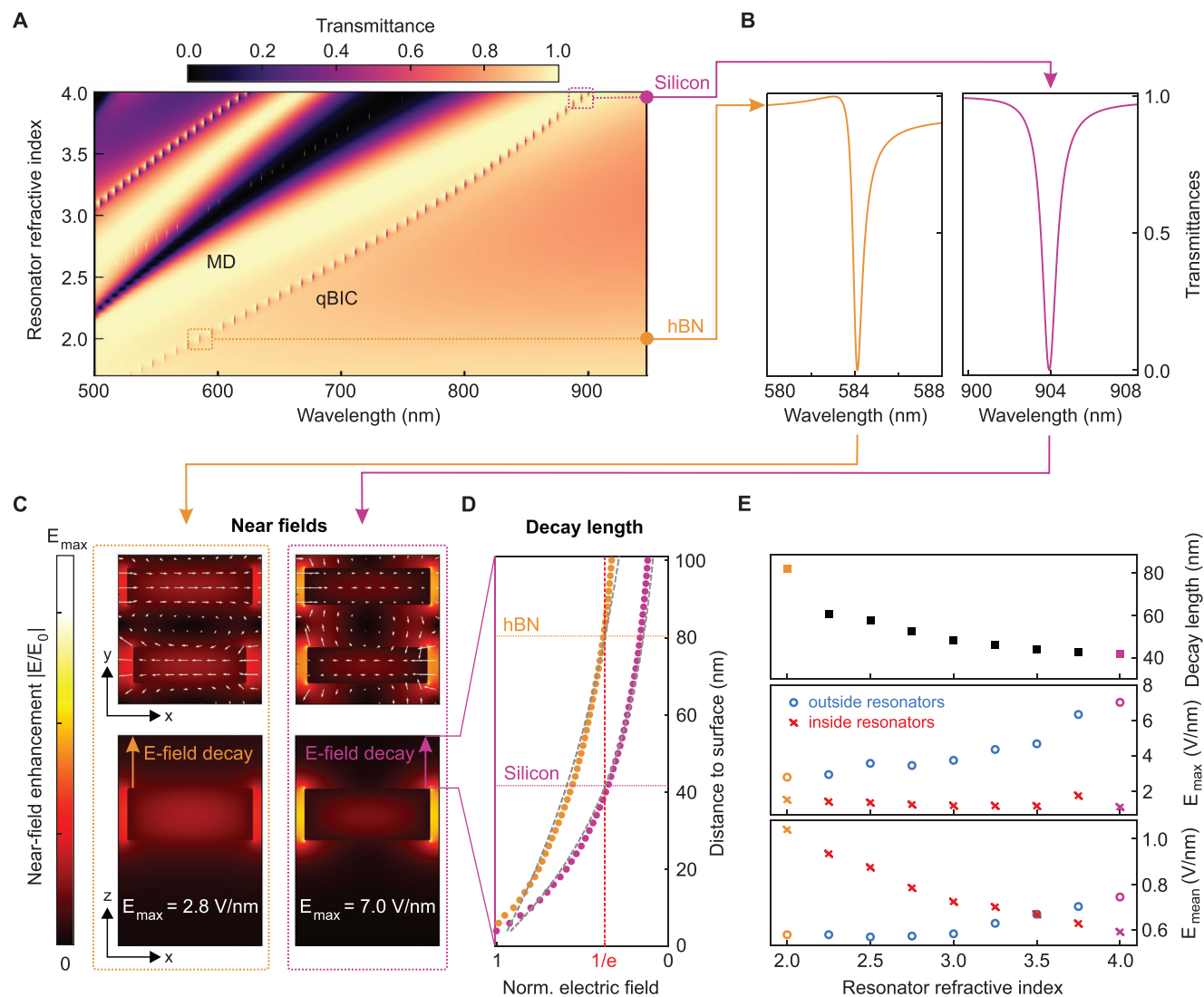


Figure 2. Impact of the resonator refractive index on the spectral and near-field properties. A) Simulated transmittance spectra for the asymmetric double rod qBIC unit cell with different resonator refractive indices, assuming the refractive index of the substrate $n_{\text{substrate}} = 1$, showing pronounced qBIC resonances along with a magnetic dipolar (MD) resonance. The resonator materials are assumed to be lossless and without dispersion throughout the spectral range of interest. B) Representative qBIC resonance spectra for refractive indices related to silicon ($n = 4$), in purple, and hBN ($n = 2$), in yellow. C) Associated qBIC near-field enhancement for the silicon and hBN case. D) Decay of the enhanced electric field away from the surface of the structure as indicated by the arrows in (C). For silicon, the decay length is smaller and the fields are mainly confined to the surface of the resonators when compared to hBN. E) Top: Decay lengths extracted for the different resonator refractive indices. Maximum value of the electric fields inside the resonators (red crosses) and outside above the substrate (blue circles) in the middle panel and mean value in the lower panel. The behavior of the mean electric fields indicates that the enhanced near fields are pushed outside the resonators for increasing resonator refractive indices. All data were simulated for $S = 1$ and ΔL was adjusted such that $Q = 1100$ for all resonances according to Equation (2).

the low-index materials reduce the requirements on the fabrication accuracy since the same geometrical asymmetries ΔL lead to lower values of the generalized asymmetry α (see Equation (2)).

Note that the metasurface design has to be carefully optimized when the spectral separation between the Rayleigh anomaly and the qBIC decreases. For the experimental situation including a substrate, this decrease is most prominent for smaller resonator refractive indices as shown in Figure S3, Supporting Information, eventually leading to a vanishing of the qBIC.

3. hBN High-Q Resonances through the Complete Visible Range to the NIR

Based on our numerical analysis above, we utilize the optimized design of the unit cell already introduced in Figure 1 for the experimental demonstration of hBN qBIC metasurfaces. For fabrication, we mechanically exfoliate monocrystalline bulk hBN from a bulk single crystal onto a fused silica (SiO_2) substrate. Suitable flakes are identified via optical microscopy and their corresponding thickness is determined with a profilometer. We utilize electron beam lithography followed by a gold

evaporation step which is used as etching mask. A liftoff and subsequent reactive ion etching process transfers the patterns into the hBN flake, before the remaining gold is removed by wet chemistry (see Experimental Section for additional details on the fabrication process). **Figure 3A** shows the corresponding grayscale microscopy image of a patterned hBN flake, where we fabricated more than 20 arrays, with varying scaling factor, from a single exfoliated crystal.

To characterize our hBN qBIC metasurfaces, we illuminate the sample with collimated white light and collect the transmitted signal with a 50× (numerical aperture (NA) = 0.8) objective. The light is coupled to a multi-mode fiber and a grating-based spectrometer where it is detected by a silicon CCD camera. In order to remove any unwanted spectral features from the sample or the beam path, we reference all our metasurface transmittance spectra to the bare SiO₂ substrate.

Figure 3B shows two representative hBN qBIC resonances for a scaling factor of $S = 0.65$ (green curve, upper panel) and $S = 1.10$ (brown curve, lower panel) with a spectral separation of almost 300 nm. Uniquely, the qBIC resonance is spectrally isolated from any other mode, highly favorable for its usage in sensing applications or light-matter interaction enhancement. As shown in **Figure 3D**, we demonstrate the full tunability range of the qBIC resonances by sweeping the scaling factor S of the unit cell to obtain a comb of well pronounced qBIC resonances throughout the complete visible spectrum extending from 413 nm far into the NIR range to 960 nm, only limited by the silicon detector efficiency, depicted in **Figure 3E**. Note that the spectra shown are individually normalized such that the maximum transmittance $T_{\max} = 1$ and the minimum transmittance $T_{\min} = 0$ (for raw data see **Figure S4**, Supporting Information). This resonance scaling corresponds to a tuning range of 1.71 eV, which is, to the best of our knowledge, the broadest qBIC-based resonance sweep reported in the literature. Remarkably, the resonant structures are all fabricated from the same flake with a height of 200 nm and the design is optimized for a single wavelength.

To further analyze the hBN qBIC resonances, we utilize a temporal coupled mode theory (TCMT) approach^[47] to fit the qBIC lineshape and extract the corresponding modulation and Q factors for each scaling factor, as shown in **Figure 3C**. We find that most qBIC resonances show Q factors above 200 with some of them exhibiting modulations exceeding 50% in the visible range. Moreover, we observe high- Q resonances below 460 nm, in particular at 413 nm, a spectral position that has not been reported in the literature, with Q factors outperforming all-dielectric- and metal-based approaches by almost one order of magnitude.^[48,49]

The extracted modulations and Q factors show their maximum values between $S = 0.8$ and $S = 1.1$ while dropping off toward lower or higher scaling factors. We attribute the decreasing Q factors and resonance modulations when approaching the blue spectral range in the visible to the onset of interband absorption in hBN, combined with fabrication-induced geometrical variations caused by the small feature size of the metasurface. Similarly, when pushing the resonances further into the NIR, the optical mode volume is mismatched with the resonator volume and, since the height of the flake is fixed, the Rayleigh anomaly will necessarily

spectrally shift toward and over the qBIC resonance, thus significantly reducing the modulation (see **Figure S5**, Supporting Information). Nevertheless, these effects could be minimized by optimizing the hBN flake height and unit cell design for each resonance position.

Beyond the scaling of the optical resonances, we demonstrate the flexibility of the qBIC design by controlling the coupling of the qBIC to the far-field via the geometrical asymmetry of the metasurface unit cell. As shown in **Figure 4A**, the Q factor increases for smaller geometrical asymmetries until the quasi-BIC transforms into a dark BIC without any far-field coupling for $\Delta L = 0$ (black dashed curve), allowing for precise tailoring of the radiative Q factor by controlling the geometrical asymmetry.

4. SHG Enhancement in hBN qBIC Metasurfaces

We further combine the versatility of the BIC-based resonances with the highly enhanced electric near fields inside the low-index hBN to demonstrate qBIC-enhanced SHG, enabling the spectrally tailored generation of light in the UV spectral region. As shown in **Figure 4B**, we utilize finite-element method simulations (COMSOL Multiphysics) to investigate the SHG efficiency for different geometrical asymmetries. As expected from qBIC metasurfaces, higher Q factors are associated with larger near-field enhancements leading to a maximum SHG efficiency for the smallest geometrical asymmetry of $\Delta L = 10$ nm (dark brown curve). Since the experimental Q factors are always limited by fabrication imperfections,^[50] we choose $\Delta L = 75$ nm as a trade-off between a high Q factor and a good resonance modulation to guarantee a large SHG enhancement.

The SHG signal in the fabricated sample is excited using a tunable Ti:sapphire laser and collected in a transmission geometry (see Experimental Section). **Figure 4C** shows the corresponding SHG signal for an hBN metasurface with $\Delta L = 75$ nm. The SHG data presented here are acquired for one array with a single qBIC resonance, but further SHG enhancement is expected for different BIC wavelengths. We observe a 388-fold qBIC-induced SHG enhancement by tuning the excitation source to the two different excitation polarizations, either parallel or perpendicular to the sample. This corresponds to the “on” and “off” states of the qBIC resonance, as shown in **Figure S6**, Supporting Information. For incident light linearly polarized along the long rod axis (E_{par} , red curve in **Figure 4C**), the qBIC is excited and promotes the SHG enhancement via the highly enhanced near fields. For perpendicularly polarized light (E_{per} , black curve in **Figure 4C**) the SHG enhancement is absent, since the qBIC is not excited in this configuration. This resonance controllability provides an important control mechanism to demonstrate qBIC-related enhancement effects and allows us to unambiguously extract an enhancement factor above 10².

As a further confirmation of the qBIC-related SHG enhancement, we sweep the excitation wavelength for the same metasurface and observe a clear correlation between the qBIC resonance (shown in solid gray in **Figure 4D**) and the SHG signal at half the qBIC resonance wavelength for a pump wavelength of 796 nm. By spectrally shifting the excitation wavelength away from the qBIC resonance to 830 nm, the SHG

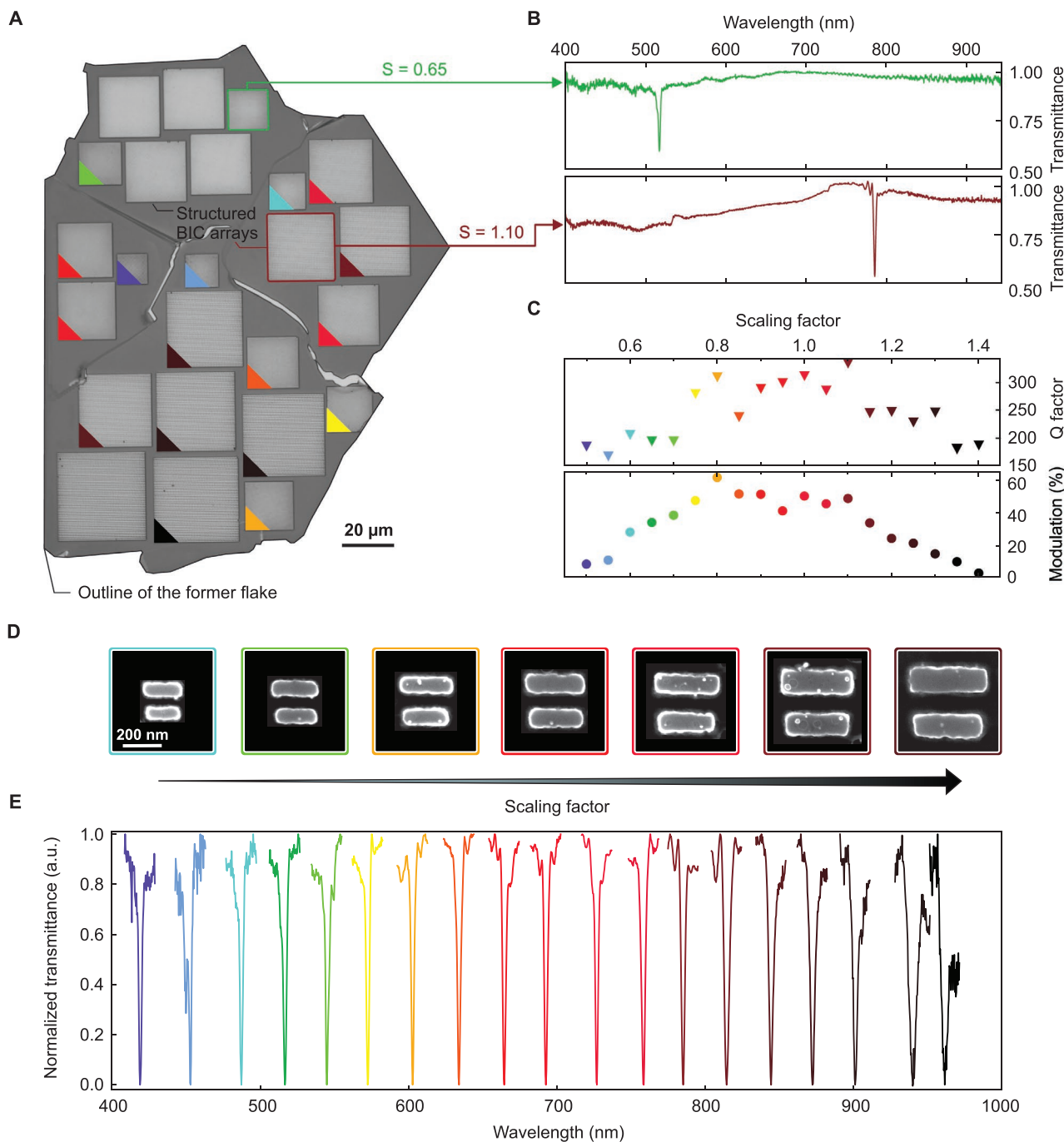


Figure 3. High- Q qBIC resonances from hBN through the visible to the NIR. A) Optical grayscale microscopy image of the bulk hBN flake along with the nanostructured qBIC arrays with different scaling factors S . B) Broad range spectra showing the spectral isolation of the qBIC for $S = 0.65$ (green curve, upper panel) and for $S = 1.10$ (brown curve, lower panel). C) Q factors and modulation depths (bottom) extracted for each resonance scaling factor (shown in (E)) indicate an optimum thickness for the utilized design. D) SEM images of qBIC unit cells for increasing scaling factor. E) High- Q qBIC resonances through the visible to the NIR obtained from a single hBN flake by increasing the scaling factor of the metasurface's unit cell.

signal intensity is largely reduced, underpinning the qBIC-driven resonant enhancement.

We further investigate the dependence of the SHG signal on the incident polarization, shown in Figure 4E for resonant ($\lambda_{\text{pump}} = 796 \text{ nm}$) and off-resonant ($\lambda_{\text{pump}} = 830 \text{ nm}$) excitation.

As expected, on resonance, the SHG signal clearly follows a fully linearly polarized pattern, with the maximum of intensity when the incident light is parallel to the long axis of the rod. On the contrary, in the off-resonant case, the SHG signal shows no polarization dependence, indicating that the SHG is caused

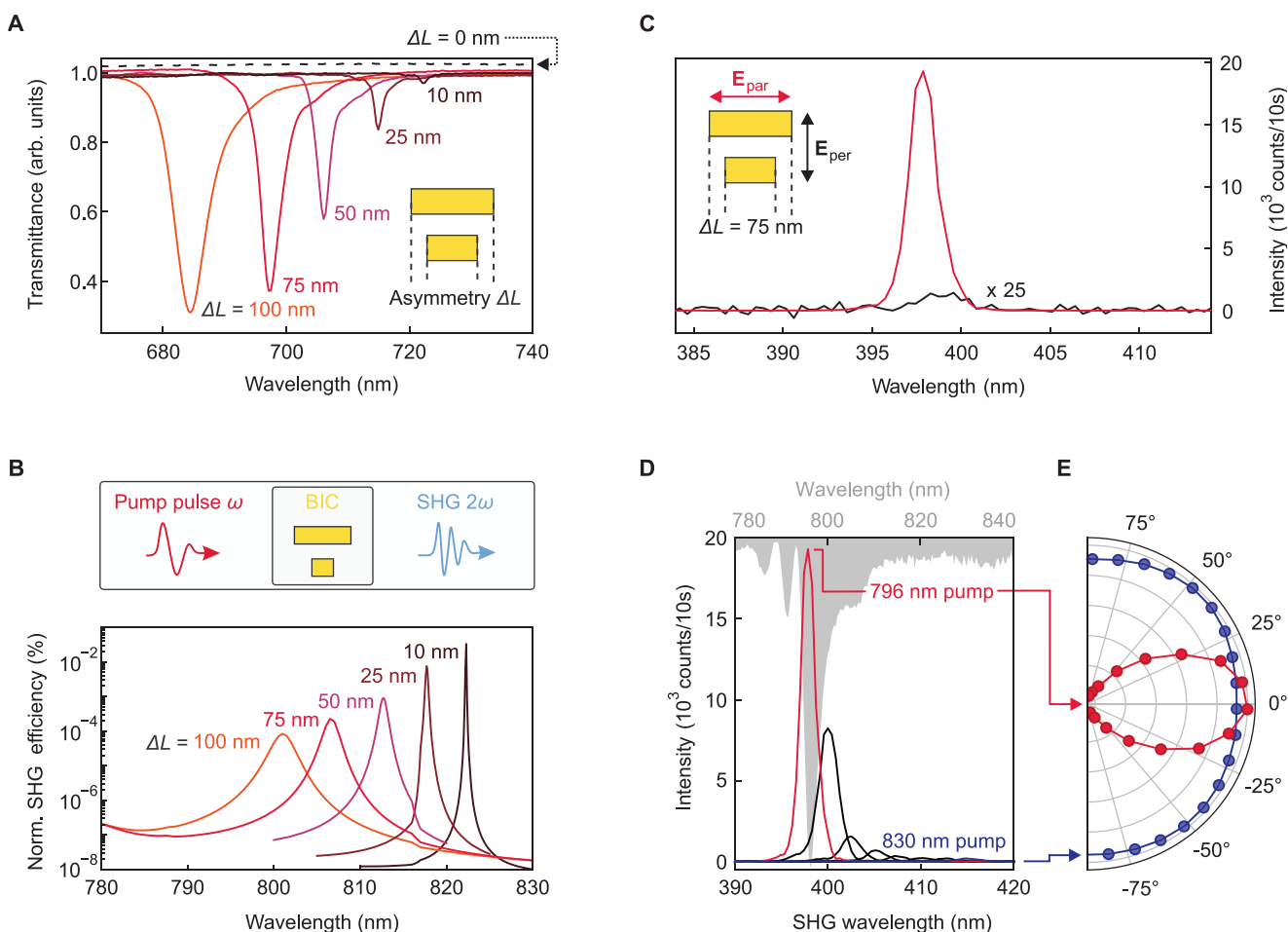


Figure 4. Symmetry-broken qBIC tuning flexibility and SHG enhancement in hBN-based qBIC metasurfaces. A) Measured optical white light transmittance spectra for hBN metasurfaces with different asymmetries ranging from $\Delta L = 100$ nm (orange curve) to symmetric structures with $\Delta L = 0$ nm (black dashed line), showing no coupling to the radiation continuum. B) Numerical simulations of the normalized SHG efficiency for different geometrical asymmetries, showing the highest enhancement for $\Delta L = 10$ nm. C) SHG signal from a qBIC metasurface with $\Delta L = 75$ nm, showing a 388-fold qBIC-induced enhancement when comparing the two excitation polarizations parallel to the long rod axis (E_{par}) and perpendicular to the long rod axis (E_{per}). D) Pump wavelength sweep for the same metasurface as in (C), showing the qBIC-resonant enhancement of the SHG. Grayscale: Optical transmittance spectrum of the qBIC metasurface with arbitrary units. E) Normalized SHG intensities for different excitation polarizations showing a linear polarization pattern for the qBIC resonance and no detectable polarization dependence for off-resonance pump.

only by the intrinsic response of the material, instead of any photonic enhancement.

5. Conclusion

We have numerically investigated and experimentally demonstrated symmetry-broken qBIC metasurfaces based on low-refractive-index monocrystalline hBN. We have analyzed the potential benefits, such as the compatibility of hBN with other materials and the higher electromagnetic fields inside the resonators, but also the drawbacks associated with low index resonators, such as the larger decay length and less field confinement outside the resonators. Furthermore, we outlined the lack of high-index materials for high- Q resonances in the visible rendering low-index materials, such as hBN, invaluable for applications in the visible spectral range. Following our numerical predictions, we realized, for the first time, a broad band

resonance sweep of 1.71 eV from the NIR through the complete visible spectral region with well isolated resonances providing Q factors above 150 (with a maximum of 314) and maximum modulations exceeding 50%. Additionally, we showed flexible tuning of the qBIC resonances using the geometrical asymmetry of the structures and the excitation polarization, giving us full control over the resonance position and Q factor. Upon resonant excitation, we utilized the highly confined electric near fields inside the hBN resonators to demonstrate a 388-fold qBIC-based SHG enhancement from hBN in the UV spectral region. Our results highlight the great promise of hBN as a resonator material when combined with the versatile radiative loss management of qBIC metasurfaces, especially for the technologically relevant visible spectral region. In particular, our hBN-based platform is ideally suited for engineering strong light-matter coupling via the integration of native single photon emitting defects in bulk hBN or in nanostructured vdW heterostructures based on atomically thin semiconductors.

6. Experimental Section

Numerical Simulations of hBN-Based qBIC Resonances: The numerical simulations of the hBN qBIC metasurfaces were performed in the frequency domain with CST Microwave using periodic boundary conditions under TE and TM excitation. If considered, the SiO₂ substrate was assumed to be lossless and the refractive index was assumed to be isotropic and non-dispersive and was thus set to 1.45. For the modeling of the hBN optical properties, Sellmaier's equations were used according to ref. [46] to account for the strong refractive index anisotropy of hBN. In particular, the equation

$$n_{\parallel}(\lambda) = \sqrt{1 + \frac{3.336 \lambda^2}{\lambda^2 - 26322}} \quad (4)$$

was used for the in-plane refractive index and

$$n_{\perp}(\lambda) = \sqrt{1 + \frac{2.263 \lambda^2}{\lambda^2 - 26981}} \quad (5)$$

for the out-of-plane refractive index. Furthermore, it was assumed that the hBN was lossless ($\kappa = 0$) throughout the spectral region of interest up to 3.4 eV (compared to 6 eV bandgap energy).

Nanofabrication of hBN qBIC Metasurfaces: Bulk hBN exfoliation crystals were obtained via high-pressure growth as described in refs. [50,51]. Single monocrystalline bulk flakes were isolated from the exfoliation crystal via mechanical exfoliation onto a silicon dioxide (SiO₂) substrate with a previously defined marker system made from chromium (Cr), which was frequently used in the literature.^[52,53] Suited flakes were identified using an optical microscope and their thicknesses were measured with a Stylus profilometer (Bruker Dektak). Afterwards, a double-layer of the positive-tone electron beam resist poly(methyl methacrylate) (PMMA, Allresist) was spun onto the sample with different chain lengths (80 nm of 950k on top of 100 nm of 495k) with soft-baking steps of 3 min at 170 °C in between. An electrically conductive polymer (Espacer 300Z) was coated on top of the resist to avoid electron charge accumulations and thus pattern distortions. The lithography pattern was defined using electron beam lithography (Raith eLine plus) with an acceleration voltage of 30 kV, aperture size of 15 μm, a working distance of 10 mm, and an area dose of 350 μC cm⁻². After the conductive polymer was washed off in a water bath for 10 s, the PMMA double layer was developed in a 3:1 isopropanol (IPA):methylisobutylketone solution for 90 s with subsequent 30 s bath in pure IPA. The metal hard-mask consisted of 2 nm titanium (Ti) as adhesion promoter and 60 nm gold (Au) which was deposited via electron beam evaporation. The sample was then left for lift-off overnight at 80 °C in a resist remover solution (Microposit remover 1165). After the lift-off process, the hard mask pattern was transferred into the hBN via inductively coupled reactive ion etching (ICP-RIE) for 50 s using SF₆ as precursor gas under 6.0 mTorr pressure with 300 W HF and 150 W ICP power. Finally, the hard mask was removed by placing the sample inside a potassium-based Au etchant and rinsing it in water afterward.

Optical Transmittance Measurements of hBN-Based qBICs: The optical characterization of the hBN-based qBIC metasurfaces was performed using a commercial white-light transmission microscopy setup (Witec Alpha series 300). The metasurfaces were excited with linearly polarized collimated white light (Thorlabs OSL2) with an illumination area of roughly 1 cm² through the backside of the sample and the collected transmitted intensity was collected with a 50× (NA = 0.8) objective. The collected light was focused into a multimode fiber and directed to a grating-based spectrometer, where the light was dispersed and directed onto a silicon CCD. Each spectrum shown herein was referenced to the bare SiO₂ substrate to eliminate unwanted spectral features from the beam path.

Determination of Resonance Q Factors: For the extraction of the resonance Q factors, TCMT^[47] was utilized and

$$T(\nu) = \left| \frac{ie^{i\phi}t_0 + \frac{\gamma_r}{\gamma_r + \gamma_i + i(\nu - \nu_{\text{res}})}}{\gamma_r + \gamma_i + i(\nu - \nu_{\text{res}})} \right|^2 \quad (6)$$

was used as fitting function. Here, $ie^{i\phi}t_0$ incorporated the background transmission and the loss rate $\gamma = \gamma_r + \gamma_i$ included the radiative (γ_r) and the intrinsic (γ_i) losses. The Q factor could then be obtained by dividing the resonance frequency ν_{res} by the loss rate:

$$Q = \frac{\nu_{\text{res}}}{2\gamma} \quad (7)$$

SHG Measurements: The SHG signal was obtained by exciting the sample with the output of a tunable Ti:sapphire laser (Coherent Chameleon Ultra II) with repetition rate of 80 MHz, for the fine tuning of the excitation wavelength to the qBIC resonance of the hBN metasurfaces. A transmission geometry was employed where the sample was excited with a low NA objective (10×, NA 0.25) with the spot size matched to the spatial dimensions of the metasurfaces, here 16.75 μm in diameter. The SHG signal was collected with a higher NA objective (40×, NA 0.6). The SHG signal was filtered with a shortpass optical filter at 680 nm (Semrock) before being analyzed by a grating-spectrometer with a silicon CCD camera (Princeton Instruments). The polarization-resolved SHG signal was obtained by inserting a halfwave plate in the excitation path.

Supporting Information

Supporting Information is available from the Wiley Online Library or from the author.

Acknowledgements

The studies were funded by the Deutsche Forschungsgemeinschaft (DFG, German Research Foundation) under grant numbers EXC 2089/1 – 390776260 (Germany's Excellence Strategy), TI 1063/1 (Emmy Noether Program), and MA 4699/7-1, the Bavarian program Solar Energies Go Hybrid (SolTech), the Center for NanoScience (CeNS). K.W. and T.T. acknowledge support from the JSPS KAKENHI (Grant Numbers 19H05790, 20H00354 and 21H05233). L.S. acknowledges funding support through a Humboldt Research Fellowship from the Alexander von Humboldt Foundation. S.A.M. additionally acknowledges the EPSRC (EP/W017075/1) and the Lee-Lucas Chair in Physics.

Open access funding enabled and organized by Projekt DEAL.

Conflict of Interest

The authors declare no conflict of interest.

Data Availability Statement

The data that support the findings of this study are available from the corresponding author upon reasonable request.

Keywords

bound states in the continuum, hexagonal boron nitride, high-Q resonances, low index photonics

Received: October 20, 2022

Revised: December 14, 2022

Published online: February 21, 2023

[1] M. Lawrence, D. R. Barton, J. Dixon, J.-H. Song, J. van de Groep, M. L. Brongersma, J. A. Dionne, *Nat. Nanotechnol.* **2020**, *15*, 956.

- [2] A. C. Overvig, S. Shrestha, S. C. Malek, M. Lu, A. Stein, C. Zheng, N. Yu, *Light: Sci. Appl.* **2019**, *8*, 92.
- [3] A. Tittl, A. Leitis, M. Liu, F. Yesilkoy, D.-Y. Choi, D. N. Neshev, Y. S. Kivshar, H. Altug, *Science* **2018**, *360*, 1105.
- [4] F. Yesilkoy, E. R. Arvelo, Y. Jahani, M. Liu, A. Tittl, V. Cevher, Y. Kivshar, H. Altug, *Nat. Photonics* **2019**, *13*, 390.
- [5] T. Shibanuma, T. Matsui, T. Roschuk, J. Wojcik, P. Mascher, P. Albella, S. A. Maier, *ACS Photonics* **2017**, *4*, 489.
- [6] J. Karst, M. Floess, M. Ubl, C. Dingler, C. Malacrida, T. Steinle, S. Ludwigs, M. Hentschel, H. Giessen, *Science* **2021**, *374*, 612.
- [7] Y. Bao, Q. Lin, R. Su, Z.-K. Zhou, J. Song, J. Li, X.-H. Wang, *Sci. Adv.* **2020**, *6*, eabh0365.
- [8] P. Huo, C. Zhang, W. Zhu, M. Liu, S. Zhang, S. Zhang, L. Chen, H. J. Lezec, A. Agrawal, Y. Lu, T. Xu, *Nano Lett.* **2020**, *20*, 2791.
- [9] H. Ren, G. Briere, X. Fang, P. Ni, R. Sawant, S. Héron, S. Chenot, S. Vézian, B. Damilano, V. Brändli, S. A. Maier, P. Genevet, *Nat. Commun.* **2019**, *10*, 2986.
- [10] H. Ren, X. Fang, J. Jang, J. Bürger, J. Rho, S. A. Maier, *Nat. Nanotechnol.* **2020**, *15*, 948.
- [11] J. Wang, J. Kühne, T. Karamanos, C. Rockstuhl, S. A. Maier, A. Tittl, *Adv. Funct. Mater.* **2021**, *31*, 2104652.
- [12] Y. Yang, I. I. Kravchenko, D. P. Briggs, J. Valentine, *Nat. Commun.* **2014**, *5*, 5753.
- [13] D. G. Baranov, D. A. Zuev, S. I. Lepeshov, O. V. Kotov, A. E. Krasnok, A. B. Evlyukhin, B. N. Chichkov, *Optica* **2017**, *4*, 814.
- [14] I. Staude, J. Schilling, *Nat. Photonics* **2017**, *11*, 274.
- [15] C. Wu, N. Arju, G. Kelp, J. A. Fan, J. Dominguez, E. Gonzales, E. Tutuc, I. Brener, G. Shvets, *Nat. Commun.* **2014**, *5*, 3892.
- [16] A. Leitis, A. Tittl, M. Liu, B. H. Lee, M. B. Gu, Y. S. Kivshar, H. Altug, *Sci. Adv.* **2019**, *5*, eaaw2871.
- [17] S. Campione, S. Liu, L. I. Basilio, L. K. Warne, W. L. Langston, T. S. Luk, J. R. Wendt, J. L. Reno, G. A. Keeler, I. Brener, M. B. Sinclair, *ACS Photonics* **2016**, *3*, 2362.
- [18] A. P. Anthur, H. Zhang, R. Paniagua-Dominguez, D. A. Kalashnikov, S. T. Ha, T. W. W. Maß, A. I. Kuznetsov, L. Krivitsky, *Nano Lett.* **2020**, *20*, 8745.
- [19] L. Hüttenhofer, M. Golibrzuch, O. Bienek, F. J. Wendisch, R. Lin, M. Becherer, I. D. Sharp, S. A. Maier, E. Cortés, *Adv. Energy Mater.* **2021**, *11*, 2102877.
- [20] T. S. Moss, *Phys. Status Solidi* **1985**, *131*, 415.
- [21] P. Hervé, L. K. J. Vandamme, *Infrared Phys. Technol.* **1994**, *35*, 609.
- [22] J. B. Khurgin, *ACS Photonics* **2022**, *9*, 743.
- [23] H. Shim, F. Monticone, O. D. Miller, *Adv. Mater.* **2021**, *33*, 2103946.
- [24] S. Sun, Z. Zhou, C. Zhang, Y. Gao, Z. Duan, S. Xiao, Q. Song, *ACS Nano* **2017**, *11*, 4445.
- [25] C. Zhang, S. Divitt, Q. Fan, W. Zhu, A. Agrawal, Y. Lu, T. Xu, H. J. Lezec, *Light: Sci. Appl.* **2020**, *9*, 55.
- [26] K.-H. Kim, I.-P. Kim, *RSC Adv.* **2022**, *12*, 1961.
- [27] K. Koshelev, S. Lepeshov, M. Liu, A. Bogdanov, Y. Kivshar, *Phys. Rev. Lett.* **2018**, *121*, 193903.
- [28] S. I. Azzam, A. V. Kildishev, *Adv. Opt. Mater.* **2021**, *9*, 2001469.
- [29] A. Kodigala, T. Lepetit, Q. Gu, B. Bahari, Y. Fainman, B. Kanté, *Nature* **2017**, *541*, 196.
- [30] M. V. Rybin, K. L. Koshelev, Z. F. Sadrieva, K. B. Samusev, A. A. Bogdanov, M. F. Limonov, Y. S. Kivshar, *Phys. Rev. Lett.* **2017**, *119*, 243901.
- [31] K. Koshelev, S. Kruk, E. Melik-Gaykazyan, J.-H. Choi, A. Bogdanov, H.-G. Park, Y. Kivshar, *Science* **2020**, *367*, 288.
- [32] B. Gil, G. Cassaboais, R. Cusco, G. Fugallo, L. Artus, *Nanophotonics* **2020**, *9*, 3483.
- [33] G. Cassaboais, P. Valvin, B. Gil, *Nat. Photonics* **2016**, *10*, 262.
- [34] F. Ferreira, A. J. Chaves, N. M. R. Peres, R. M. Ribeiro, *J. Opt. Soc. Am. B* **2019**, *36*, 674.
- [35] H. Xu, B. Ding, Y. Xu, Z. Huang, D. Wei, S. Chen, T. Lan, Y. Pan, H.-M. Cheng, B. Liu, *Nat. Nanotechnol.* **2022**, *17*, 1091.
- [36] C. R. Dean, A. F. Young, I. Meric, C. Lee, L. Wang, S. Sorgenfrei, K. Watanabe, T. Taniguchi, P. Kim, K. L. Shepard, J. Hone, *Nat. Nanotechnol.* **2010**, *5*, 722.
- [37] S. J. Haigh, A. Gholinia, R. Jalil, S. Romani, L. Britnell, D. C. Elias, K. S. Novoselov, L. A. Ponomarenko, A. K. Geim, R. Gorbachev, *Nat. Mater.* **2012**, *11*, 764.
- [38] Y. Liu, N. O. Weiss, X. Duan, H.-C. Cheng, Y. Huang, X. Duan, *Nat. Rev. Mater.* **2016**, *1*, 16042.
- [39] M. Autore, P. Li, I. Dolado, F. J. Alfaro-Mozaz, R. Esteban, A. Atxabal, F. Casanova, L. E. Hueso, P. Alonso-González, J. Aizpurua, A. Y. Nikitin, S. Vélez, R. Hillenbrand, *Light: Sci. Appl.* **2018**, *7*, 17172.
- [40] M. Autore, I. Dolado, P. Li, R. Esteban, F. J. Alfaro-Mozaz, A. Atxabal, S. Liu, J. H. Edgar, S. Vélez, F. Casanova, L. E. Hueso, J. Aizpurua, R. Hillenbrand, *Adv. Opt. Mater.* **2021**, *9*, 2001958.
- [41] J. D. Caldwell, I. Aharonovich, G. Cassaboais, J. H. Edgar, B. Gil, D. N. Basov, *Nat. Rev. Mater.* **2019**, *4*, 552.
- [42] J. D. Caldwell, A. V. Kretinin, Y. Chen, V. Giannini, M. M. Fogler, Y. Francescato, C. T. Ellis, J. G. Tischler, C. R. Woods, A. J. Giles, M. Hong, K. Watanabe, T. Taniguchi, S. A. Maier, K. S. Novoselov, *Nat. Commun.* **2014**, *5*, 5221.
- [43] S. Kim, J. E. Fröch, J. Christian, M. Straw, J. Bishop, D. Totonjian, K. Watanabe, T. Taniguchi, M. Toth, I. Aharonovich, *Nat. Commun.* **2018**, *9*, 2623.
- [44] J. E. Fröch, Y. Hwang, S. Kim, I. Aharonovich, M. Toth, *Adv. Opt. Mater.* **2019**, *7*, 1801344.
- [45] A. K. Geim, I. V. Grigorieva, *Nature* **2013**, *499*, 419.
- [46] Y. Rah, Y. Jin, S. Kim, K. Yu, *Opt. Lett.* **2019**, *44*, 3797.
- [47] S. Fan, W. Suh, J. D. Joannopoulos, *J. Opt. Soc. Am. A* **2003**, *20*, 569.
- [48] X. Zhu, G. M. I. Hossain, M. George, A. Farhang, A. Cicek, A. A. Yanik, *ACS Photonics* **2020**, *7*, 416.
- [49] M. Semmlinger, M. L. Tseng, J. Yang, M. Zhang, C. Zhang, W.-Y. Tsai, D. P. Tsai, P. Nordlander, N. J. Halas, *Nano Lett.* **2018**, *18*, 5738.
- [50] J. Kühne, J. Wang, T. Weber, L. Kühner, S. A. Maier, A. Tittl, *Nanophotonics* **2021**, *10*, 4305.
- [51] T. Taniguchi, K. Watanabe, *J. Cryst. Growth* **2007**, *303*, 525.
- [52] T. Weber, L. Kühner, L. Sortino, A. B. Mhenni, N. P. Wilson, J. Kühne, J. J. Finley, S. A. Maier, A. Tittl, *arXiv:2209.01944*, **2022**.
- [53] R. Verre, D. G. Baranov, B. Munkhbat, J. Cuadra, M. Käll, T. Shegai, *Nat. Nanotechnol.* **2019**, *14*, 679.